Extrusion dynamics of deep-water volcanoes revealed by 3D seismic data

Qiliang Sun[1,2,3], Christopher A.L. Jackson[4], Craig Magee[4], and Xinong Xie[1,3]

[1]Key Laboratory of Tectonics and Petroleum Resources, China University of Geosciences (Wuhan), Ministry of Education, Wuhan 430074, China;

[2]Laboratory for Marine Mineral Resources, Qingdao National Laboratory for Marine Science and Technology, Qingdao 266061, China;

[3]College of Marine Science and Technology, China University of Geosciences (Wuhan), Wuhan, Hubei 430074, PR China;

[4]Basins Research Group (BRG), Department of Earth Science & Engineering, Imperial College, London, SW7 2BP, UK

Abstract

Difficulties in imaging the exterior and interior of deep-water volcanoes mean their extrusion dynamics remain poorly understood. We use 3D seismic reflection data to determine the geometry, distribution, and extrusion dynamics of two Late Miocene-Quaternary, deep-water (emplaced in >1.6 km water depths) volcanoes in the South China Sea. The volcanoes erupted lava flows that fed lobate fans, with the former associated with >9 km long lava tubes. The basal contacts of the lava flows are rugged and display erosional ramps with heights of up to 57±8 m. Importantly, c. 50-97% of the total erupted volume is preserved in these long run-out lava flows. Estimates of erupted lava volumes are therefore likely erroneous if based solely on mapping the top surface of an edifice and/or associated lava flows. We suggest the deep-water environment of eruption, which is likely characterized by high hydrostatic pressures and soft near-seabed sediment, influenced extrusion dynamics.

Keywords

Volcanism, lava flow channel, lava fan, lava tube, sill, South China Sea

1. Introduction

The external morphology of volcanoes and their eruptive products reflect, and provide insights into, the processes controlling magma extrusion and volcano construction. By extracting high-resolution, quantitative data on the morphology of modern and, in some cases, still active volcanic edifices and surrounding lava fields from airborne/shuttle radar topography or time-lapse multi-beam bathymetry, we can estimate erupted volume and reconstruct volcano growth (e.g. Holcomb et al., 1988; Walker, 1993; Goto and McPhie, 2004; Cocchi et al., 2016; Somoza et al., 2017; Allen et al., 2018; Grosse and Kervyn, 2018). Whilst remote sensing data capture the external morphology of volcanoes and lava flows, they do not image their basal surface or internal architecture. Without access to the full 3D structure of these extrusive systems, it is difficult to assess the accuracy of estimated volumes of erupted material, or test volcano growth and lava emplacement models.

Several studies demonstrate that seismic reflection data can be used to map the external morphology and internal architecture of buried volcanoes in 3D (e.g. Planke et al., 2000; Calvès et al., 2011; Jackson, 2012; Magee et al., 2013; Reynolds et al., 2017). To date, the majority of these studies have focused on volcanoes formed in sub-aerial or shallow-marine environments (e.g. Planke et al., 2000; Jackson, 2012; Magee et al., 2013; Reynolds et al., 2018). The 3D geometry, internal structure and volume of deep-water volcanoes located along the continental margins thus remain poorly documented.

In this study, we use high-resolution 3D seismic reflection data to examine two, Late Miocene-Quaternary submarine volcanoes emplaced in deep-water (>1.6 km) on highly stretched continental lithosphere in the northern South China Sea (Fig. 1). Based on interpretation of volcano and lava flow structure, distribution, and scale, we discuss emplacement processes and relate our findings to studies of deep-water volcanoes that use bathymetry and ROV data. Importantly, we show basal surfaces of volcanoes and lava flows are rugged, meaning volume estimates assuming a smooth base are likely oversimplified. We conclude that volcano and lava field morphology are controlled by the physical (e.g. high hydrostatic pressure, unconsolidated seafloor sediments) and geomorphic (e.g. slope dips) occurring along many deep-water margins, and that the volcano edifices themselves may comprise only a small part of the total erupted magma volume.

2. Geological setting

The study area is located in the Pearl River Mouth Basin, on the northern continental slope of the South China Sea (Fig. 1a). The South China Sea was an area of subduction in the late Mesozoic, before the onset of continental rifting and subsequent seafloor spreading in the Cenozoic (e.g. Taylor and Hayes, 1983; Franke et al., 2014; Li et al., 2014; Sun et al., 2014a; Ding and Li, 2016). A lack of seaward dipping reflections (SDRs), and low volumes of rift-related igneous rocks, suggest the northern part of the South China Sea is as a magma-poor margin (Yan et al., 2006; Franke, 2013). Seafloor spreading ceased at ~15-15.5 Ma (Briais et al., 1993; Li et al., 2014), with post-rift thermal cooling driving subsidence of the northern South China Sea margin since the Early Miocene (Yu, 1994). During this phase of thermal subsidence, the Philippine Arc collided with the Eurasian continental margin at ~5.5 Ma (Hall, 2002), promoting magmatism, uplift, and normal faulting around the Dongsha Islands (i.e. the Dongsha Event; Lüdmann et al., 2001).

Volcanoes associated with post-rift magmatism were emplaced both onshore and offshore (e.g. Zou et al., 1995; Yan et al., 2006; Franke, 2013; Li et al., 2014; Sun et al., 2014b; Zhao et al., 2014, 2016; Fan et al., 2017), with the latter typically extruded onto continental slope sedimentary rocks in relatively shallow water depths (<300 m; Yan et al., 2006; Zhao et al., 2016). Boreholes reveal these relatively shallow-water volcanoes are composed of basalt, dacite, and rhyolitic tuff (Li and Liang, 1994; Yan et al., 2006; Zhao et al., 2016).

In addition to the shallow-water volcanoes, during the Late Miocene-Quaternary several volcanoes were emplaced further basinwards on the continental slope, close to the Continent-Ocean Boundary (COB) (Fig. 1). These volcanoes are situated in an area currently characterized by water depths of 1970-2680 m and a mean, broadly southward dip of >1° (Fig. 1). Data (microfauna) from nearby ODP sites 1145, 1146, and 1148 reveal that, since the Middle Miocene (~16.5 Ma), sedimentation in the study area has been dominated by deposition of a deep-marine (>1.6 km water depth), nanofossil-bearing clay (Wang et al., 2000; Clift et al., 2001).

These borehole observations suggest Late Miocene-Quaternary volcanoes near the COB were emplaced in relatively deep waters (>1.6 km).

3. Data and Methods

We use a time-migrated 3D seismic reflection survey acquired in 2012 and covering an area of ~350 km^2 (Fig. 1b). The seismic data are zero-phase processed and displayed with SEG (Society of Exploration Geophysicists) normal polarity, whereby a downward increase in acoustic impedance (a function of rock velocity and density) corresponds to a positive reflection event (red on seismic profiles) (Figs. 2a-2b) (e.g. Brown, 2004; Jackson et al., 2010). Bin spacing is 25 m, and the seismic data have a dominant frequency in the interval of interest (0-300 m) of ~40 Hz. Stacking velocities are not available for this study and no wells lie within the area of interest; because of this, we have no direct control on the velocities of the seismically imaged volcanic materials that would allow us to convert measurements in milliseconds two-way time (ms TWT) to meters. However, based on velocity data for rocks of assumed similar composition, we can estimate the velocities of imaged volcanic materials and provide a range of likely values (Text S1). Note that the estimated velocities used here do not affect the *ratio* between material contained within the edifice and the flanking lava flows (Text S1). We calculate a vertical resolution ($\lambda/4$) of ~10 m for sediments (nanofossil-bearing clay) and 19-25 m for volcanic materials, assuming seismic velocities of 1540 m/s for the sedimentary strata (based on nearby ODP Site 1146 data; Fig. 1) (Sun et al., 2017) and 3500±500 m/s for volcanic materials (Text S1). The top and base of volcanic structures can be distinguished in seismic reflection data when their thickness is greater than the estimated vertical resolution of these data (i.e. 19-25 m); volcanic structures with thicknesses below the vertical resolution, but above the detection limit (i.e. $\lambda/8$ = 10-13 m,) are imaged as tuned reflection packages (i.e. their top and base contacts cannot be determined). We interpreted six seismic surfaces that we correlate to ODP Site 1146 (Figure S1), which is located ~65 km west of the study area: T0 (~2.58 Ma); T1 (~5.3 Ma); TRa (~6.5 Ma); TRb (~8.2 Ma), and TM and BM, which correspond to the top and base of the volcanic materials, respectively. After mapping the TM and BM, the volumes of the volcanic products are calculated (Table S1-S4), with errors largely arising from uncertainties in the velocities (3500±500 m/s) used to undertake the depth conversion (see above). RMS (root mean square) amplitude extractions, and slices though variance volume (Text S2) are used to reveal the geometry, scale, and distribution of the submarine volcanoes (Figs. 2-3).

4. Seismic expression of magmatic products

We identify two main types of seismic structures and associated facies: (1) Seismic Facies 1 (SF1) - two (V1 and V2) conical-shaped features up to 353.5±50.5 m high, which internally are only weakly to moderately reflective, and capped by a positive polarity, high-amplitude reflection (Figs. 2a, 3c, S2); and (2) Seismic Facies 2 (SF2) - ribbon-like, broadly strata-concordant, high-amplitude, positive polarity reflections, which emanate from the conical structures and extend up to ~9.2 km downslope (Figs. 2a-2b, 3c, S2). SF1 is similar in terms of its conical shape, highly reflective top, and internally chaotic reflections to mud volcanoes documented elsewhere in the northern South China Sea (Sun et al., 2012; Yan et al., 2017). Furthermore, the highly reflective, ribbon-like geometry of SF2 is similar to that associated with shallow/free gas accumulations (Sun et al., 2012). However, we consider these two interpretations unlikely because: (i) the limited supply and high viscosity of mud means mud volcanoes are rarely associated with long run-out flows such as these documented here (i.e. >9 km; see below); and (ii) the top of SF2 is defined by a positive polarity reflection (downward increase in acoustic impedance), which is opposite to that typically associated with shallow/free gas accumulations (e.g. Judd and Hovland, 2007; Sun et al., 2012). Based on their geometric and geophysical characteristics, spatial relationships, and geometrical and geophysical similarity structures observed on other continental margins, we interpret these features as volcanic edifices (SF1) and genetically related lava flows (SF2) (e.g. Planke et al., 2000; Thomson and Hutton, 2004; Calvès et al., 2011; Jackson, 2012; Magee et al., 2013; Reynolds et al., 2018). We now focus on the detailed external forms and internal architectures of two deep-water volcanoes that are shallowly buried (<150 m) and thus well-imaged.

4.1. Volcano edifice 1 (V1) and associated lava flows

V1 is a prominent conical structure covering ~7.2 km^2, with a volume of ~0.82±0.12 km^3 (i.e.

assuming seismic velocities of 3500±500 m/s) and an average flank dip of ~13.2±1.8° (Fig. 2; Table S1). Where continuous reflections occur within V1, they lie sub-parallel to its flanks, and converge down-dip towards the surface BM, onto which they downlap (Fig. 2a). V1 is onlapped by overlying reflections, with the oldest onlapping reflection correlating to TRa (~6.5 Ma); this suggests V1 is latest Miocene-earliest Pliocene (Fig. 2a). A downward-tapering, up to 2.0 km wide, sub-vertical zone of chaotic reflections underlies V1 (Fig. 2a).

V1 is surrounded by an asymmetric apron of moderate-to-high amplitude reflections that extend up to 1.5 km from the main edifice, and which are up to 202±29 m thick (Figs. 2c-d) (Table S2). A package of moderate-to-very high-amplitude reflections extend a further c. 1.5 km down-dip of this apron (Figs 1b, 2c). In detail, the latter package contains very high-amplitude, channel-like geometries that terminate down-dip into or are flanked at prominent bends by, moderate-amplitude, fan-like geometries; we interpret these two features as lava flow channels (C1-C3) and fans (F1-F4), respectively (Fig. 2). The lava flow channels are sinuous, <340 m wide, and usually bisect the lava fans (Figs 2c-d). Together, lava flow-related features (i.e. apron, channels, and fans) emanating from V1 cover an area of ~14 km^2 (Tables S3-S4), have an average thickness of ~57.2±7.9 m, and thus have a volume of ~0.81±0.12 km^3; this volume is ~99% of the volume of V1 (~0.82±0.12 km^3) and ~50% of the total erupted volume.

4. 2. Volcano edifice 2 (V2) and associated lava flows

V2 is elliptical in plan-view, with a long and short axis of ~1.2 km and ~0.6 km, respectively (Fig. 3a-b). Its flanks dip 26.4±3.3º and it is smaller than V1, covering only ~0.44 km^2 (volume of 0.02-0.03 km^3) (Fig. 3a; Table S1). The top of V2 is of moderate amplitude and is irregular, with the oldest onlapping reflections correlating to T1 (~5.3 Ma); this suggests V2, like V1, is latest Miocene-earliest Pliocene (Fig. 3c). Reflections within V2 are chaotic, and, similar to V1, it is underlain by a vertical zone of disturbance (Fig. 3c). V2 lacks a lava apron, instead being directly flanked by relatively straight, up to 9.2 km long lava flow channels on its south-eastern side (C4-C7) (Fig. 3a). Lava flow C6 is unusual in that underlying strata are truncated at the base of the flow, defining 'ramps' that are up to ~56.8±7.9 m high and dip at ~23.5±3.0º (Figs. 3d-e1). Beyond the main ramp (Fig. 3b), the lava flows thickens to 226.7±32.1 m, where it is defined by stacked, high-amplitude reflections that have a lobate geometry in plan-view (F5) (Figs. 3a, 3c, 3e-e1). At its distal end, the pinchout of F5 is defined by abutment against another basal ramp (Figs. 3e-e1). F5 is capped by a younger, adjacent lava fan (F6) (Figs. 3e-e1, Text S2). The V2-sourced lava flows (C4-C7 and F5) cover ~11.5 km^2 (~4.20 km^2 of lava flow channels and ~7.32 km^2 of lava fan). Given the average thickness of the lava flow channels (~52.5±7.5 m) and fans (~94.5±13.5 m), we calculate the total volume of V2-sourced lava flows to be 0.92±0.13 km^3; this value is ~37 times greater than the volume of the main V2 edifice (0.025±0.005 km^3), representing ~97% of the total erupted volume.

5. Discussion

5.1. Deep-water extrusion dynamics

We show that volcanoes are typically either flanked by an asymmetric lava apron, which is broader on their downslope (SE) side, or lava flow channels that flowed south-eastwards (Figs. 2a, c-d, 3a). These observations suggest local slope, of only a few degrees (c. 1°), controls the direction of lava flow, with those fed by particularly voluminous eruptions able to flow several tens of kilometers (e.g. C5 and C6; Figs. 2c, 3a). Similar to subaerial volcanoes (e.g. Walker, 1993; Cashman et al., 1999) and mid-oceanic ridge volcanoes (e.g. Caress et al., 2012), high eruption rates and low magma viscosities may generate long run-out flows. However, long run-out lava flows are rarer in submarine than subaerial environments due to relatively rapid cooling and hardening of magma upon contact with seawater (e.g. Holcomb et al., 1988). We propose that, in addition to eruption onto a slope, the formation of lava tubes (Greeley, 1987) was a key control on lava run-out distance. These tubes formed as magma flowed downslope, with hardening of its surface and formation of a solidified crust preventing further heat loss within the tube core. Moreover, the crystallization of lava would release latent heat, which could, to some extent, compensate for the heat lost via surficial cooling (Miles and Cartwright, 2010). Extrusion into relatively deep water (i.e. a few kilometers) may also have played a role in driving the formation of long run-out lava flows. At these depths, high hydrostatic pressure (>16 MPa) inhibits degassing and fragmentation, causing lava to maintain its low viscosity and flow further (Gregg and Fornari, 1998). Lava flow run-out may also have been facilitated by the sustained pressure from newly erupting lava emanating from the source volcano.

Lava flow eventually ceased in distal areas due to gradual cooling and crystallization of the erupted melt (Cashman et al., 1999). We suggest that, in the case of the straight lava flows (C5 and 6), lava transported from within the axial tube temporarily accumulated at the transient end of the flow, possibly forming a lava pool (Greeley, 1987). Lava entering the tube from the ongoing or new volcanic eruption caused an increase in pressure, with the cooled and crystallized material at the flow toe forming an impermeable, albeit transient barrier. Eventually, pressure buildup was sufficient to rupture this frontal barrier, leading to emplacement of a fan downdip of the frontmost base-lava ramp (F5; Fig. 3a, c-d1) (Griffiths, 2000). However, in the case of fans (e.g. F1-4) fed by sinuous channels (Figs. 2c-d), we suggest these were emplaced in a process similar to that documented by Miles and Cartwright (2010), with lobate lava flows fed and bisected by a 'lava tube' through magma inflation. At the end of sinuous lava flow channels (e.g. C1), the main channel bifurcated to form a lobate fan (F3, Figs. 2c-d), which was also probably caused by flow branching triggered by magma cooling (Griffiths, 2000).

The overall geometry and internal architecture of the imaged lava flows indicate substrate rheology was a key control on emplacement dynamics. For example, the base-lava ramps suggest these flows were able to erode down into the seabed, likely because the pre-eruption substrate was cold, wet, and unconsolidated. We suggest that, by being denser, the lava flow was able to sink down into or 'dredge' the soft sediments (Duffield et al., 1986), with the high temperatures also permitting thermal erosion of substrate by intra-flow turbulence (Griffiths, 2000).

5.2. Comparison to shallow-water and subaerial extrusion dynamics

Our 3D seismic reflection data show that relatively long run-out lava flows erupted from deep-water volcanoes formed and were emplaced above, an overall rugged basal surface that is locally defined by discrete erosional basal 'ramps'. These flows are not confined by this basal relief, typically passing downdip into lava flow fans (Figs. 2-3). Lava flows erupted from subaerial and shallow-water volcanoes also run-out for long distances (>10 km), and display superficially similar geometric features to these documented here (e.g. lava flow channels/'tubes', downdip lava fans, overall thin, sheet-like flows; e.g. Greeley, 1987; Cashman et al., 1999; Thomson, 2005; Caress et al., 2012; Planke et al., 2017; Reynolds et al., 2017, 2018). The local accumulation of lava in 'pools' is also common in subaerial, shallow-water, and deep-water environments, although in the first two cases they are usually trapped within lakes or pre-existing low relief (Greeley, 1987; Cashman et al., 1999; Griffiths, 2000), rather than formed, syn-eruption, by thermal erosion and magma sinking as documented here in deep-water (Fig. 3c). The geometric similarities between lavas erupted from subaerial and shallow-water settings suggest that, in the latter, the low hydrostatic pressure does not greatly influence the lava physical properties (e.g. viscosity) or the overall dynamics of lava flow emplacement. Subaerial and shallow-water volcanoes may however differ in that the edifices of latter may be better-preserved due to rapid post-formation sediment blanketing and burial, which protects it from erosion (Walker, 1993; Jackson, 2012).

Compared to lavas erupted from subaerial and shallow-water volcanoes, the basal contacts of those erupted from deep-water volcanoes are likely more irregular due to thermal erosion, and less degassing and fragmentation of magma caused by the high hydrostatic pressures (Gregg and Fornari, 1998; Griffiths, 2000) (Fig. 3c). Lava flow channel 'excavation' is rarely observed in subaerial environments, likely because older flows, comprised of strong, igneous rock, are resistant to erosion. However, the lack of lava flow channel 'excavation' in shallow-water settings is perhaps unexpected, given flows are emplaced on a cold, wet, unconsolidated seabed (e.g. Thomson, 2005; Planke et al., 2017; Reynolds et al., 2017). Their absence may reflect the fact that: (1) due to a lower confining pressure, volatiles escape more readily from shallow-water lava flows, promoting heat exchange between the lava and seawater, causing the former to cool more quickly and reduce its ability to thermally erode the seabed; (2) the density contrast between the erupted materials and background sediments is less (i.e. lava erupted in shallow-water contains more voids and may thus be of lower density than less porous and thus denser lavas erupted in deeper water; e.g. White et al., 2015); and/or (3) such features do occur in shallow-water settings, but that they simply have not been observed because of limited 3D seismic reflection data coverage or quality.

5.3. Volume balance of volcano edifice and lava flow

High-resolution 3D seismic reflection data allow us to calculate the volumes of material contained within volcano edifices and in flanking lava flows. We show that most (i.e. 50-97%) of the erupted material is transported away from the imaged volcanoes, an observation comparable to that made for subaerial fall deposits (Pyle, 1989), and deep-ocean volcanic eruptions (Caress et al., 2012; Carey et al., 2018). Importantly, we show that the flanking lava flows in particular do not have concordant bases, but can instead erode into underlying sediment during extrusion (Fig. 3c); accurately calculating their volume therefore requires an understanding of the basal morphology of such flows. Our results therefore suggest that erupted magma volume estimates based solely on remote sensing of the seabed may be incorrect (e.g. Robinson and Eakins, 2006). The underestimation of total erupted magma volumes would compromise our understanding of storage conditions, eruption rates, eruption durations, and associated risk assessments of submarine volcanism (Carey et al., 2018).

6. Conclusions

High-resolution 3-D seismic data allow us to image and map the internal structure, and to better understand the extrusion dynamics of, and to calculate the total amount of material erupted from deep-water volcanoes; such insights cannot readily be gained from analysis of remote sensing data. High hydrostatic pressure, an inclined seabed, and low-strength, very fine-grained, near-seabed sediments, combined with formation of lava tubes and extrusion of low-viscosity magmas, are likely responsible for anomalously long-distance lava run-out in this deep-water environment. Moreover, we show that a large amount (as high as ~97%) of the erupted materials are transported away from the volcano edifices, suggesting that volume of deep-water volcanic edifices may not faithfully archive eruption size or magma production. This study complements the shallow-water/subaerial achievements using seismic reflection data to study the internal structures and extrusion dynamics of magma. It strengths that the original extrusive environments play important roles on the magma extrusion dynamics and associated morphologies. Considering the deep-water conditions (e.g. inclined slope and unconsolidated sediments) in the study area are common elsewhere, the conclusions derived from this study can probably be used in other deep-water sedimentary basins and some mid-ocean ridges. This study also highlights that 3D seismic reflection data are required to understand the volcano morphology in 3D and estimate volume of volcanic materials.

Acknowledgment

This work was supported by the National Scientific Foundation of China (Grant Nos. 91528301, 41676051 and 41372112), the Programme of Introducing Talents of Discipline to Universities (No. B14031) and the Fundamental Research Funds for the Central Universities-the China University of Geosciences (Wuhan) (No. CUG160604). We thank the China National Offshore Oil Company for permission to release the data. The reflection seismic data may be requested from this Company. We thank Dr. Dieter Franke and Dr. Dennis Brown for their invaluable comments on the original version of this paper. Dr. Rebecca Bell is thanked for generously providing office space during the visit of Dr. Qiliang Sun to Imperial College.

References

Allen, R.W., Berry, C., Henstock, T.J., Collier, J.S., Dondin, F.J-Y., Rietbrock, A., Latchman, J.L., and Robertson, R.E.A., 2018, 30 Years in the Life of an Active Submarine Volcano: A Time - Lapse Bathymetry Study of the Kick-'em-Jenny Volcano, Lesser Antilles: Geochemistry, Geophysics, Geosystems, v. 19, p. 715-731, doi: doi.org/10.1002/2017GC007270.

Briais, A., Patriat, P., and Tapponnier, P., 1993, Updated interpretation of magnetic anomalies and seafloor spreading stages in the South China Sea: Implications for the Tertiary tectonics of Southeast Asia: Journal of Geophysical Research, v. 98, p. 6299-6328, doi:10.1029/92JB02280.

Brown, A. R., 2004, Interpretation of three-dimensional seismic data: AAPG Memoir 42, 6thed. SEG Investigations in Geophysics.

Calvès, G., Schwab, A.M., Huuse, M., Clift, P.D., Gaina, C., Jolley, D., Tabrez, A.R., and Inam, A., 2011, Seismic volcanostratigraphy of the western Indian rifted margin: The pre-Deccan igneous province: Journal of Geophysical Research, v. 116, p. B01101, doi: 10.1029/2010JB000862.

Caress, D.W., Clague, D.A., Paduan, J.B., Martin, J.F., Dreyer, B.M., Chadwick Jr, W.W., Denny, A., and Kelley, D.S., 2012, Repeat bathymetric surveys at 1-metre resolution of lava flows erupted at Axial Seamount in April 2011: Nature Geoscience, v. 5, p. 483-488, doi: 10.1038/NGEO1496.

Carey, R., Soule, S.A., Manga, M., White, J.D.L., McPhie, J., Wysoczanski, R., Jutzeler, M., Tani, K., Yoerger, D., Fornari, D., Caratori-Tontini, F., Houghton, B., Mitchell, S., Ikegami, F., Conway, C., Murch, A., Fauria, K., Jones, M., Cahalan, R., and McKenzie, W., 2018. The largest deep-ocean silicic volcanic eruption of the past century: Science Advances, v. 4, p. e1701121, doi: 10.1126/sciadv.1701121.

Cashman, K.V., Thornber, C.R., and Kauahikaua, J.P., 1999, Cooling and crystallization of lava in open channels, and the transition of pahoehoe lava to `a`a: Bulletin of Volcanology, v. 61, p. 306-323, doi: 10.1007/s004450050.

Clift, P.D., Lin, J., and ODP Leg 184 Scientific Party, 2001, Patterns of extension and magmatism along the continent-ocean boundary, South China margin: Geological Society, London, Special Publications, v. 187, p. 489-510, doi: 10.1144/GSL.SP.2001.187.01.24.

Cocchi, L., Masetti, G., Muccini, F., and Carmisciano, C., 2016, Geophysical mapping of Vercelli Seamount: Implications for Miocene evolution of the Tyrrhenian back arc basin: Geoscience Frontiers, v. 7, p. 835-849, doi: 10.1016/j.gsf.2015.06.006.

Ding, W.W., and Li, J.B., 2016, Propagated rifting in the Southwest Sub-basin, South China Sea: Insights from analogue modelling: Journal of Geodynamics, v. 100, p. 71-86, doi:10.1016/j.jog.2016.02.004.

Duffield, W.A., Bacon, C.R., and Delaney, P.T., 1986, Deformation of poorly consolidated sediment during shallow emplacement of a basalt sill, Coso Range, California: Bulletin of Volcanology, v. 48, p. 97-107, doi: 10.1007/BF01046545.

Fan, C.Y., Xia, S.H., Zhao, F., Sun, J.L., Cao, J.H., Xu, H.L., and Wan, K.Y., 2017, New insights into the magmatism in the northern margin of the South China Sea: Spatial features and volume of intraplate seamounts: Geochemistry, Geophysics, Geosystems, v. 18, p. 2216-2239, doi: 10.1002/2016GC006792.

Franke, D., 2013, Rifting, lithosphere breakup and volcanism: comparison of magma-poor and volcanic rifted margins: Marine and Petroleum Geology, v. 43, p. 63-87.

Franke, D., Savva,D., Pubellier, M., Steuer, S., Mouly, B., Auxietre, J., Meresse, F., and Chamot-Rooke, N., 2014, The final rifting evolution in the South China Sea: Marine and Petroleum Geology, v. 58, p. 704-720.

Goto, Y., and McPhie, J., 2004, Morphology and propagation styles of Miocene submarine basanite lavas at Stanley, northwestern Tasmania, Australia: Journal of Volcanology and Geothermal Research, v. 130, p. 307-328.

Grosse, P., and Kervyn, M., 2018, Morphometry of terrestrial shield volcanoes: Geomorphology, v. 304, p. 1-14, doi: 10.1016/j.geomorph.2017.12.017.

Greeley, R., 1987, The role of lava tubes in Hawaiian volcanoes, U.S. Geological Survey Professional Paper 1350, p. 1589-1602.

Gregg, T.K.P., and Fornari, D.J., 1998, Long submraine lava flows: Observations and results from numerical modeling: Journal of Geophysical Research, v. 103, p. 27517-27531, doi: 10.1029/98JB02465.

Griffiths, R.W., 2000, The Dynamics of lava flows: Annual Review of Fluid Mechanics, v. 32, p. 477-518, doi: 10.1146/annurev.fluid.32.1.477.

Hall, R., 2002. Cenozoic geological and plate tectonic evolution of SE Asia and the SW Pacific: Computer-based reconstructions, model and animations. Jounarl of Asian Earth Sciences, 20: 353-431.

Holcomb, R.T., Moore, J.G., Lipman, P.W., and Belderson, R.H., 1988, Voluminous submarine lava flows from Hawaiian volcanoes: Geology, v. 16, p. 400-404, doi: 10.1130/0091-7613(1988)016<0400:VSlava flow fanH>2.3.CO;2.

Jackson, C.A.-L., 2012, Seismic reflection imaging and controls on the preservation of ancient sill-fed magmatic vents: Journal of the Geological Society, London: v. 169, p. 503-506, doi: 10.1144/0016-76492011-147.

Judd, A.G., and Hovland, M., 2007, Seabed Fluid Flow: The Impact on Geology, Biology and the Marine Environment. Cambridge University Press, Cambridge, pp. 163-178.

Li, C.F., Xu, X., Lin, J., Sun, Z., et al., 2014, Ages and magnetic structures of the South China Sea constrained by the deep tow magnetic surveys and IODP Expedition 349: Geochemistry, Geophysics, Geosystems, v. 15, p. 4958-4983.

Li, P., and Liang, H., 1994. Cenozoic magmatism in the Pearl River Mouth Basin and its relationship to the basin evolution and petroleum accumulation: Guangdong Geology, v. 9, p. 23-34 (in Chinese with English abstract).

Lüdmann, T., Wong, H.K., and Wang, P., 2001, Plio-Quaternary sedimentation processes and neotectonics of the northern continental margin of the South China Sea: Marine Geology, v. 172, p. 331-356.

Magee, C., Hunt-Stewart, E., and Jackson, C.A.-L., 2013, Volcano growth mechanisms and the role of sub-volcanic intrusions: Insights from 2D seismic reflection data. Earth and Planetary Science Letters, v. 373, p. 41-53, doi: 10.1016/j.epsl.2013.04.041.

Miles, A., and Cartwright, J., 2010, Hybrid fl ow sills: A new mode of igneous sheet intrusion: Geology, v. 38, p. 343-346, doi: 10.1130/G30414.1.

Planke, S., Millett, J.M., Maharjan, D., Jerram, D.A., Abdelmalak, M.M., Groth, A., Hoffmann, J., Berndt, C., and Myklebust, R., 2017, Igneous seismic geomorphology of buried lava fields and coastal escarpments on the Vøring volcanic rifted margin: Interpretation, v. 5, p. SK161–SK177, doi: 10.1190/INT-2016-0164.1.

Planke, S., Symonds, P., Alvestad, E., and Skogseid, J., 2000, Seismic volcanostratigraphy of large-volume basaltic extrusive complexes on rifted margins: Journal of Geophysical Research, v. 105, p. 19335-19351, doi: 10.1029/1999JB900005.

Pyle, D.M., 1989. The thickness, volume and grainsize of tephra fall deposits: Bulletin of Volcanology, v. 51, p. 1-15, doi: 10.1007/BF01086757.

Reynolds, P., Holford, S., Schofield, N., and Ross, A., 2017, Three-dimensional seismic imaging of ancient submarine lava flows: an example from the southern Australian margin: Geochemistry, Geophysics, Geosystems, v. 18, p. 3840-3853, doi: 10.1002/2017GC007178.

Reynolds, P., Schofield, N., Brown, R.J. and Holford, S.P., 2018, The architecture of submarine monogenetic volcanoes-insights from 3D seismic data: Basin Research, v. 30, p. 437-451, doi: 10.1111/bre.12230.

Robinson, J.E., and Eakins, B.W., 2006, Calculated volumes of individual shield volcanoes at the young end of the Hawaiian Ridge: Journal of Vocanology and Geothermal Research, v. 151, p. 309-617, doi: 10.1016/j.jvolgeores.2005.07.033.

Sibuet, J.-C., Yeh, Y.-C., and Lee, C.-S., 2016. Geodynamics of the South China Sea: Tectonophysics, v. 692, p. 98-119, doi:10.1016/j.tecto.2016.02.022

Somoza, L., Gonzalez, F.J., Barker, S.J., Madureira, P., Medialdea, T., de Ignacio, C., Lourenco, N., Leon, R., Vazquez, J.T., and Palomino, D., 2017. Evolution of submarine eruptive activity during the 2011-2012 El Hierro event as documented by hydroacoustic images and remotely operated vehicle observations: Geochemistry, Geophysics, Geosystems, v. 18, p. 3109-3137, doi: 10.1002/2016GC006733.

Sun, Q.L., Xie, X.N., Piper, D.J.W., Wu, J., and Wu, S.G., 2017, Three dimensional seismic anatomy of multi-stage mass transport deposits in the Pearl River Mouth Basin, northern South China Sea: Their ages and kinematics: Marine Geology, v. 393, p. 93-108, doi: 10.1016/j.margeo.2017.05.005.

Sun, Q.L., Wu, S.G., Cartwright, J., Wang, S.H., Lu, Y.T., Chen, D.X., and Dong, D.D., 2014b, Neogene igneous intrusions in the northern South China Sea: evidence from high resolution three dimensional seismic data: Marine and Petroleum Geology, v. 54, p. 83-95.

Sun, Q.L.,Wu, S.G., Cartwright, J., and Dong, D.D., 2012, Shallow gas and focused fluid flow systems in the Pearl River Mouth Basin, northern South China Sea: Marine Geology, v. 315-318, p. 1-14.

Sun, Z., Xu, Z., Sun, L., Pang, X., Yan, C., Li, Y., Zhao, Z., Wang, Z., Zhang, C., 2014a. The mechanism of post-rift fault activities in Baiyun Sag, Pearl River Mouth basin. Journal of Asian Earth Sciences, 89:76-87.

Taylor, B., Hayes, D.E., 1983. Origin and history of the South China Sea Basin. In: Hayes, D.E. (Ed.), The Tectonic and Geologic Evolution of Southeast Asian Seas and Islands. AGU, Washington, DC, pp. 23-56.

Thomson, K., 2005, Volcanic features of the North Rockall Trough: Application of visualisation techniques on 3D seismic reflection data: Bulletin of Volcanology, v. 67, p. 116-128.

Thomson, K., and Hutton, D., 2004, Geometry and growth of sill complexes: Insights using 3-D seismic from the North Rockall Trough: Bulletin of Volcanology, v. 66, p. 364–375, doi: 10.1007/s00445-003-0320-z.

Wang, P., Prell, W.L., and ODP 184 scientists., 2000, Proceedings of the Ocean Drilling Program, Initial Reports, 184. Ocean Drilling Program, College Station, TX 2000.

Walker, G.P.L., 1993, Basaltic-volcano systems. In Magmatic Processes and Plate Tectonics, edited by Pritchard, H.M., Alabaster, T., Harris, N.B.W., Neary, C.R., Geological Society Special Publication, 76: 3-38.

White, J.D.L., McPhie, J., and Soule, S.A., 2000, Submarine lavas and hyaloclastite. In: Sigurdsson, H., Houghton, B.F., McNutt, S.R., Rymer, H., Stix, J. (eds), Encyclopedia of volcanoes, 2nd edn. Academic, London, pp 363–375, doi: 10.1016/B978-0-12-385938-9.00019-5

Yan, P., Deng, H., Liu, H.L., Zhang, Z., and Jiang, Y., 2006, The temporal and spatial distribution of volcanism in the South China Sea region: Journal of Asian Earth Sciences, v. 27, p. 647-659, doi: 10.1016/j.jseaes.2005.06.005.

Yan, P., Wang, Y.L., Liu, J., Zhong, G.J., and Liu, X.J., 2017, Discovery of the southwest Dongsha Island mud volcanoes amid the northern margin of the South China Sea: Marine and Petroleum Geology, v. 88, p. 858-870, doi: 10.1016/j.marpetgeo.2017.09.021.

Yang, S., Qiu, Y., and Zhu, B., 2015, Atlas of Geology and Geophysics of the South China Sea: China Navigation Publications, Tianjin.

Yu, H.S., 1994. Structure, stratigraphy and basin subsidence of Tertiary basins along the Chinese southeastern continental margin. Tectonophysics, 253, 63-76.

Zhao, F., Alves, T.M., Wu, S.G., Li, W., Huuse, M., Mi, L.J., Sun, Q.L., Ma, B.J., 2016. Prolonged post-rift magmatism on highly extended crust of divergent continental margins (Baiyun Sag, South China Sea). Earth and Planetary Science Letters, 445: 79-91.

Zhao, F., Wu, S.G., Sun, Q.L., Huuse, M., Li, W., Wang, Z.J., 2014. Submarine volcanic mounds in the Pearl River Mouth Basin, northern South China Sea. Marine Geology, 355: 162-172.

Zou, H., Li, P., Rao, C., 1995. Geochemistry of Cenozoic volcanic rocks in Zhu Jiangkou basin and its geodynamic significance. Geochimica, 24: 33-45.

Figure Captions

Figure 1: Geological setting of the study area. (a) Bottom left: regional setting of the South China Sea that is bounded by the Red River Strike-slip faults (RRFs) to the west and by the subduction trench (Manila Trench) to the east. The study area (marked with red square) is located to the south of Dongsha Islands. The green dashed line outlines the boundary of Pearl River Mouth Basin. ODP sites 1145, 1146 and 1148 are labeled. COB = Continent ocean boundary (Adopted from Sibuet et al., 2016). The base map is modified from Yang et al. (2015); (b) Seabed morphologies of the study area. Distributions of volcano edifices (red), sills (blue), lava flows (green) and locations of Figures 2c, 3a and S3a are labeled. The contour lines are in 100 ms (twt).

Figure 2: Seismic characteristics of deep-water volcano (V1) and associated lava flow channels/fans. (a) Seismic profile crosscuts the volcano edifice and associated lava flow. See Figure S2 for the un-interpreted version of this profile; (b) Seismic profile crosscuts the lava flow (enhanced seismic anomalies). TM = top of volcano/lava flow; BM = base of volcano/lava flow; (c) and (d) RMS amplitude map (± 30 ms along the surface BM) and its interpretations. Volcanic apron, lava flow channels/fans are labeled.

Figure 3: Seismic characteristics of lava flow channels/fans fed by V2 and S1/S2. (a) and (b) Variance slice (extracted from the surface BM) and its interpretations; (c) Seismic profile crosscuts V2 and along lava flow channel (C6) and Lava fans (F5 and F6). The V2 has a sharp boundary to the upslope. (d) and (d1) Enlargement of the end of lava flow channel (ramp structure) and its line drawings; (e) and (e1) Enlargement and its line drawings of the lava fans (F5 and F6). TM = top of volcano/lava flow; BM = base of volcano/lava flow; See Figure S2 for the un-interpreted version of these profiles.

Figure 1

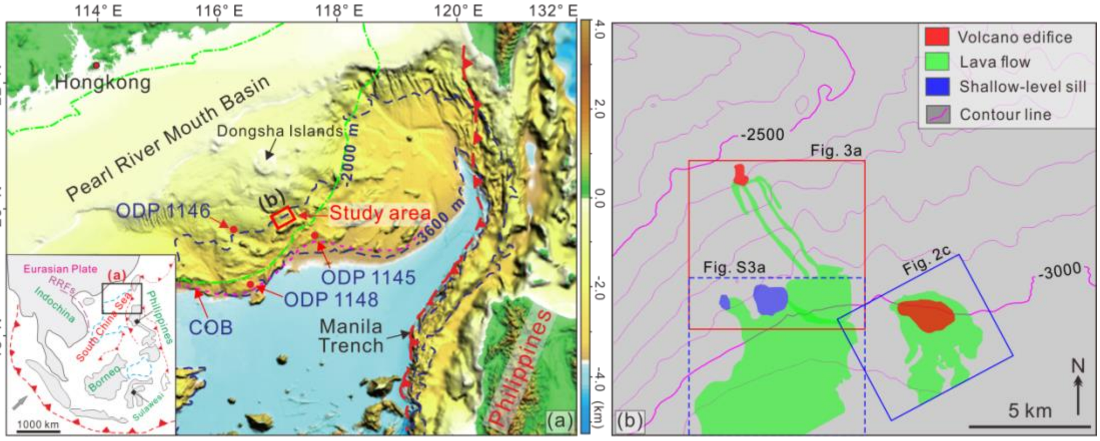
114° E
116° E
118° E
120° E
132° E
22° N
20° N
18° N
Hongkong
Pearl River Mouth Basin
Dongsha Islands
2000 m
3600 m
(b)
Study area
ODP 1146
ODP 1145
ODP 1148
COB
Manila Trench
Philippines
Eurasian Plate
(a)
RRFs
Indochina
South China Sea
Borneo
Sulawesi
1000 km
4.0
2.0
0.0
-2.0
-4.0
(km)
(a)
Volcano edifice
Lava flow
Shallow-level sill
Contour line
-2500
Fig. 3a
Fig. S3a
Fig. 2c
-3000
N
5 km
(b)

Figure 2

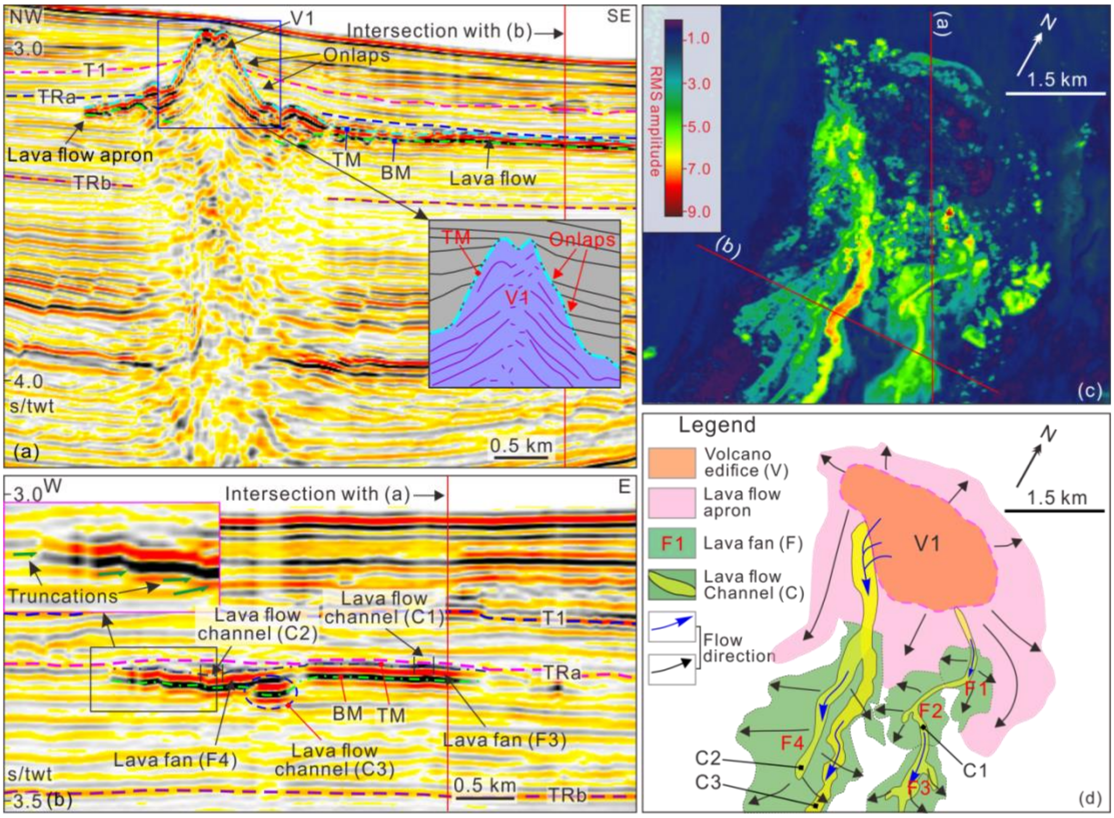

NW
SE
3.0
V1
Intersection with (b)
Onlaps
T1
TRa
Lava flow apron
TM
BM
Lava flow
TRb
TM
Onlaps
V1
4.0
s/twt
(a)
0.5 km
RMS amplitude
-1.0
-3.0
-5.0
-7.0
-9.0
(a)
(b)
N
1.5 km
(c)
W
E
3.0
Intersection with (a)
Truncations
Lava flow channel (C2)
Lava flow channel (C1)
T1
TRa
BM
TM
Lava fan (F4)
Lava flow channel (C3)
Lava fan (F3)
s/twt
0.5 km
3.5
(b)
TRb
Legend
Volcano edifice (V)
Lava flow apron
F1 Lava fan (F)
Lava flow Channel (C)
Flow direction
N
1.5 km
V1
F1
F2
F4
C1
C2
C3
F3
(d)

Figure 3

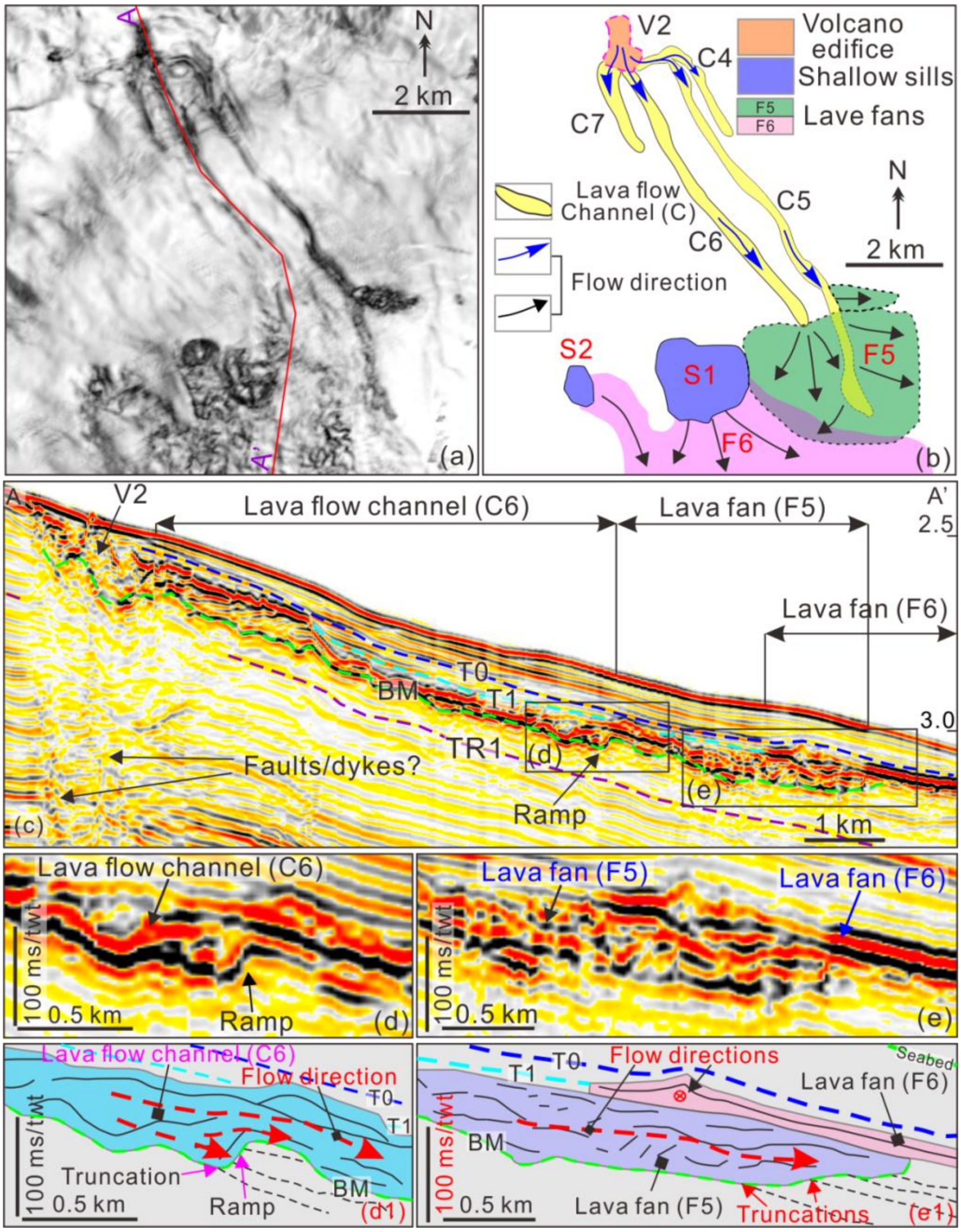

A
A'
N
2 km
(a)
V2
C4
C7
C5
C6
Volcano edifice
Shallow sills
F5
F6
Lave fans
Lava flow Channel (C)
Flow direction
S2
S1
F5
F6
(b)
A
V2
Lava flow channel (C6)
Lava fan (F5)
A'
2.5
Lava fan (F6)
T0
BM
T1
3.0
TR1
(d)
(e)
Faults/dykes?
Ramp
1 km
(c)
Lava flow channel (C6)
100 ms/twt
0.5 km
Ramp
(d)
Lava fan (F5)
Lava fan (F6)
100 ms/twt
0.5 km
(e)
Lava flow channel (C6)
Flow direction
T0
T1
100 ms/twt
Truncation
0.5 km
Ramp
BM
(d1)
T0
T1
Flow directions
Seabed
Lava fan (F6)
100 ms/twt
BM
0.5 km
Lava fan (F5)
Truncations
(e1)